Title

Novel method for ozone isopleth construction and diagnosis for ozone control strategy of Chinese cities

Authors

Huizhong Shen[1,2,5]*, Zhe Sun[3,5], Yilin Chen[1,2], Armistead G. Russell[2], Yongtao Hu[2], Mehmet Talât Odman[2], Yu Qian[2], Alexander T. Archibald[3], Shu Tao[4]

Affiliations

[1]School of Environmental Science and Engineering, Southern University of Science and Technology, Shenzhen 518055, China.

[2]School of Civil and Environmental Engineering, Georgia Institute of Technology, Atlanta, Georgia 30332, United States.

[3]Centre for Atmospheric Science, Yusuf Hamied Department of Chemistry, University of Cambridge, Cambridge CB2 1EW, UK.

[4]College of Urban and Environmental Sciences, Laboratory for Earth Surface Processes, Sino-French Institute for Earth System Science, Peking University, Beijing 100871, P.R. China.

[5]These authors contributed equally to the article.

*Corresponding author. Email: shenhz@sustech.edu.cn

ABSTRACT

Ozone (O_3) isopleths describe the non-linear responses of O_3 concentrations to changes in nitrogen oxide (NO_X) and volatile organic compounds (VOCs), and thus are pivotal to the determination of O_3 control requirements. In this study, we innovatively use the Community Multiscale Air Quality model with High-order Decoupled Direct Method (CMAQ-HDDM) to simulate O_3 pollution of China in 2017 and derive O_3 isopleths for individual cities. Our simulation covering the entire China mainland suggests severe O_3 pollution as 97% of the residents experienced at least one day, in 2017, in excess of Chinese Level-II Ambient Air Quality Standards for O_3 as 160 $\mu g \cdot m^{-3}$ (81.5 ppbV equally). The ambient O_3 concentration in China measured in the population-weighted average, is overall VOC-determinant as reducing VOC emissions shall be more effective for O_3 mitigation than controlling NO_X. However, the O_3 responses to emissions of precursors vary widely across individual cities. Densely populated metropolitan areas such as Jing-Jin-Ji, Yangtze River Delta, and Pearl River Delta are following NO_X-saturated regimes, where a small amount of NO_X reduction increases O_3. Ambient O_3 pollution in the eastern region generally are limited by VOCs, while the western regions are limited by NO_X. The city-specific O_3 isopleths generated in this study are instrumental in forming hybrid and differentiated strategies for O_3 abatement in China.

INTRODUCTION

Tropospheric ozone (O_3) is a trace gas and major air pollutant with adverse impacts on human and ecosystem health.[1] Human exposure to O_3 is associated with increased risks of respiratory and circulatory disease and premature death.[1-3] Elevated ground-level O_3 also reduces crop production and warms the atmosphere.[4] China is experiencing worsening O_3 pollution in recent years.[5] The Global Burden of Disease reported 1.8×10^5 premature deaths in China in 2017 from exposure to ambient O_3, which is the highest among all countries (and the third highest in terms of the attributable mortality rate).[6] Both large-scale surface measurements and satellite observations show that O_3 levels in China are growing,[7, 8] especially in eastern China, a region that is densely populated, with an annual increase rate of approximately 1–3 parts per billion by volume (ppbV).[7, 9, 10]

Unlike most other air pollutants that are directly emitted, ambient O_3 is formed indirectly from photochemical reactions between nitrogen oxides (NO_X) and volatile organic compounds (VOCs) in the presence of sunlight.[1] In many countries, emissions of NO_X and VOCs are regulated for O_3 control.[11, 12] The O_3 responses to NO_X and VOC reduction, however, are not linear,[13] and in certain circumstances (e.g., in the presence of high NO_X), reducing NO_X can increase O_3 because "NO_X titration" is reduced.[14, 15] This O_3-NO_X-VOC relationship conforms to a general pattern and can be illustrated with an isopleth diagram, referred to as "O_3 isopleths", where emissions or initial concentrations of NO_X and VOCs define two different axes perpendicular to each other, and the corresponding O_3 levels form the isopleths.[16-18] O_3 isopleths are widely used as a basis to diagnose O_3 trends in response to precursors' emission changes[19] and are key to the development of control strategies for O_3 reduction.[20]

There are two major conventional approaches to draw O_3 isopleths for a given locality, 1) developing

empirical relationships based on observational data[21-25] or, more commonly, 2) predicting O_3 changes using numerical models.[26-33] While empirical approaches can be fast and effective, application of these approaches is limited by the availability of measurements in space and time. In contrast, modeling approaches, especially those using three-dimensional chemical transport models (CTMs), are often computationally expensive but have the advantage of high spatial and temporal continuity and can be applied to various locations and spatial scales.[26-30, 33]

Many studies have used CTMs to generate O_3 isopleths.[33-35] A traditional method, perceived as "brute force" approach, repeats CTM simulations with altered emission inputs and is one of the commonly used approaches to calculating O_3 isopleths.[35] However, to cover a wide range of emission changes and ensure accuracy, this approach may need hundreds of simulations, which substantially increases the computational burden.[22] With recent model development, advanced sensitivity analysis techniques have been incorporated in CTMs.[36-38] Hakami et al., for example, first implemented the high-order decoupled direct method (HDDM)—a forward sensitivity analysis technique—in a CTM and successfully generated O_3 isopleths by running the model just once.[39] HDDM implemented in CTMs provides first- and second-order forward sensitivities that depict both linear and nonlinear responses of model outputs (i.e., concentrations, deposition, etc.) to input parameters (e.g., emissions, meteorology, boundary conditions, reaction rates, etc.) and is an ideal tool to examine the non-linearity of O_3 chemistry.[40, 41] Compared to the brute-force approach, using HDDM to develop O_3 isopleths requires less computing time and avoids numerical noises that have been found in applying brute-force.[28, 42] Under a large change in precursor emissions (e.g., by ±50%), however, a single application of HDDM may fail to capture the O_3 responses because the sensitivities provided by HDDM are local.[43] Several recent studies have used weighting factors to

combine multiple HDDM simulations with altered emissions to cover emission changes beyond ±50%.[44, 45] However, this weighting approach (or "stepwise approach" named in some studies) is subject to artificial parameterization, and the weighting options strongly affects the patterns of the generated O_3 isopleths. In addition, this approach cannot maintain the continuity of the first- and second-order sensitivities. The accuracy of the O_3 isopleths generated by this approach, thus, degrades significantly with increasing non-linearity of the system.[45] So far, there is still a lack of reliable and universally applicable approach to combining multiple HDDM simulations to generate O_3 isopleths.

Here, using the Community Multiscale Air Quality Modeling model with HDDM (CMAQ-HDDM), we develop a novel approach, the High-order Integral Method (HIM), to generate O_3 isopleths by fully exploiting the information provided by multiple HDDM simulations (METHODS). By integrating the multiple simulation ensemble, HIM maintains the continuity of the first- and second-order sensitivities of the generated O_3 isopleths, covers a wide range of changes in NO_X and VOC emissions (from 0% to 150%), and shows the best performance in developing O_3 isopleths among existing approaches (RESULTS AND DISCUSSION). By applying this approach, we investigate the O_3-NO_X-VOCs relationship across China in 2017, the year that a series of promulgated clean air actions set goals for.[46] We focus on ambient O_3, measured by the population-weighted O_3 concentrations ($C_{O3,pop,}$ see METHODS for the calculation), because of its stronger relevance to population-wide human health, compared to spatially-averaged metrics.[47] Through the investigation of the O_3 isopleths generated by CMAQ-HDDM, this study examines how O_3 pollution has and will respond to emissions changes and will inform further strategies for O_3 mitigation in China. The general innovations of this study lie in 1) the realistic interpretations and policy implications of the

first- and second-order sensitivities simulated from CMAQ-HDDM; 2) the HIM approach being able to generate the O_3 isopleths by respecting the atmospheric chemistry mechanism instead of just statistically interpolating; and 3) the HIM approach being able to plot the O_3 isopleths by multi-order mathematical integrations from an arbitrary single starting point in the NO_X-VOC emission coordinate system. It should be noted that there are other factors likely associated with the O_3 pollution in China, such as the reductions in particulate matter concentrations,[7] which are beyond the scope of this study.

METHODS

Model configuration

We use CMAQv5.0.2 with HDDM to simulate ground-level O_3 concentrations and calculate both the first- and second-order sensitivities (including the second-order cross sensitivity) of O_3 concentrations to anthropogenic emissions of NO_X and VOCs. Gas-phase chemistry is modeled with the CB05 chemical mechanism[48] which has been extensively evaluated in terms of photochemistry and widely used to simulate O_3 production.[49-51] The study domain covers East Asia (Figure S1) with 124×184 horizontal grid cells resolved at a 36-*km* planar horizontal resolution and 13 vertical layers extending to ~16 *km* above ground. A previous study showed that compared to finely-resolved CMAQ-HDDM simulations, coarse resolutions yield similar predictions of average ozone sensitivity on regional scales but may fail to capture sensitivity features in urban areas.[52] For example, VOC sensitivities tend to be underpredicted in urban areas by coarse resolutions.[52] Given the high computational expense of running CMAQ-HDDM, we chose 36-*km* as a compromise. How the model resolution affects O_3 isopleths warrants further investigation.

A one-year simulation using the CMAQ base model is conducted for evaluation and spans the whole

2017 year. To minimize computational costs, simulations using CMAQ-HDDM only span the period from April 1st, 2017 to October 31st, 2017. These seven months generally cover the high O_3 days across China and is defined as the O_3 season in this study. Initial and dynamic boundary conditions are derived from the Hemispheric CMAQ simulations for the same study period.[53, 54] The meteorological and emission inputs used to drive CMAQ-HDDM are adopted from an online operational air quality forecasting system, called "AiMa".[55, 56] In the AiMa modeling system, the meteorological data are generated from the Weather Research and Forecasting (WRF) model version 3.4.1[57] driven by the 0.5° global weather forecast products produced by the National Centers for Environmental Prediction (NCEP) Global Forecast System (GFS).[58] The emission inventory adopted by AiMa (called the AiMa emission inventory) is derived and used in this study. The first version of the AiMa emission inventory, split into eight source categories (i.e., agriculture, fugitive dust, residential and commercial, solvent usage, transportation, biomass burning, industry, and power plants), was developed based on activity data for year 2013 reported by China Energy Statistical Yearbook[59] and adjusted using scaling factors derived from performance evaluation of initial simulation results.[60, 61] Emissions from regions outside of China were derived from the Intercontinental Chemical Transport Experiment-Phase B emission inventory.[62] Since 2013, air pollutants concentrations in China have been decreasing year by year due to increasingly more stringent controls. To maintain a reliable air quality forecast, the AiMa emission inventory has been continuously updated using a variety of methods and techniques, such as incorporating most recent activity data, replacing with more detailed finer-scale emission inventories (in Sichuan Basin for example), adjusting by a trail-and-error method based on ground-level measurements, and adjusting by inverse modeling based on satellite observations. The purpose of these updates and adjustments

was to ensure high accuracy of the air quality forecast. In this study, we use the 2017 version of the AiMa inventory for simulations. The total anthropogenic emissions of NO_X and VOCs in China in 2017 are estimated to be 21.2 and 28.5 $Tg \cdot yr^{-1}$, respectively, in line with the estimates reported by the Multi-resolution Emission Inventory for China (MEIC) as 22.0 and 28.6 $Tg \cdot yr^{-1}$, respectively.[63] CMAQ-HDDM is designed to calculate the semi-normalized first- and second-order sensitivities of O_3 concentrations to anthropogenic NO_X and VOC emissions. The sensitivity coefficients are expressed in the same units as concentrations (ppbV) as follows,

$$S_V = \frac{\partial C_{O_3}}{\partial \varepsilon_V} \quad \text{Eq. 1}$$

$$S_N = \frac{\partial C_{O_3}}{\partial \varepsilon_N} \quad \text{Eq. 2}$$

$$S_{VV} = \frac{\partial^2 C_{O_3}}{\partial \varepsilon_V^2} \quad \text{Eq. 3}$$

$$S_{NN} = \frac{\partial^2 C_{O_3}}{\partial \varepsilon_N^2} \quad \text{Eq. 4}$$

$$S_{VN} = \frac{\partial^2 C_{O_3}}{\partial \varepsilon_V \partial \varepsilon_N} \quad \text{Eq. 5}$$

where the subscripts $_V$, $_N$, and $_{O3}$ denote VOCs, NO_X, and O_3, respectively; C_{O3} denotes O_3 concentration; ε_V and ε_N denote relative perturbations in total anthropogenic emissions of VOCs and NO_X in China, respectively; S_V and S_N are the first-order sensitivities of O_3 concentrations to VOC and NO_X emissions, respectively; S_{VV} and S_{NN} are the second-order sensitivities of O_3 concentrations to VOC and NO_X emissions, respectively; S_{VN} is the second-order cross sensitivity of O_3 concentrations to VOC and NO_X emissions. These sensitivities are local in terms of mathematical differentiation, representing how concentrations respond to changes under currently set precursor emission conditions in the nonlinear photochemical system. In our simulations, the input parameter

for ε_N is the sum of the total anthropogenic emissions of NO, NO_2, and HONO in China; the parameter for ε_V is the sum of the total anthropogenic emissions of all non-methane VOC species as defined in CB05 mechanism (Section S1 and S2 in the Supporting Information) in China.[48] By definition, the O_3 sensitivities calculated by these CMAQ-HDDM simulations depict the O_3 responses to total NO_X and VOC emissions in China. Given that O_3 may respond differently to emissions in local, surrounding, and faraway areas, the O_3 sensitivities represent the net responses of O_3 to precursors' emissions from all areas. Such nationwide configuration has been adopted in studies that investigate O_3 sensitivities to precursors emissions using DDM or other sensitivity analysis approaches.[31, 41]

Model evaluation

We evaluate the model performance by comparing modeled O_3 with ground-level measurements (Figure S2). The normalized mean bias (NMB) of the O_3-season mean MDA8h O_3 at the 1504 monitoring sites[64] across the country is -4.8%, and the Pearson correlation coefficient (r) is 0.76 (Figure S2), suggesting good agreement. Detailed results of the model evaluation for MDA8h O_3 and other compounds, including NO_X, CO, $PM_{2.5}$, PM_{10}, SO_2, and VOC, are illustrated in Figures S3–S7. Overall, the model well reproduces the temporal trends of the concentrations of multiple pollutants in each region but shows low biases in absolute levels of the concentrations. The largest disparity between modeled and observed concentrations is found for CO which has NMB of -67% (Figure S2). Such an underestimation bias in modeled CO has been commonly found and reported by other studies[65-67] and is likely associated with the inconsistency of spatial resolutions between observations and simulations and an underestimation in CO emissions.[67] The high winter levels are affected by domestic coal combustion, as CO concentrations originate roughly 50% from direct

burning emissions, most of which are local emissions, so that spatial grid-based modeling will unreasonably average the CO level inside each simulation cell.[68] Besides, the ground-based monitoring stations are usually deployed near the high population density regions, hence the observations might not credibly reflect the grid-average level. Underestimation of background CO is another possible reason for the low biases in modeled CO. Figure S2 shows that modeled CO are biased low at both high and low concentration sites. A fraction of the sites with low concentrations are regional background sites. The low biases at these sites suggest the underestimation of background CO. The underestimation of background CO is further supported by the similarity of the variations in observed and simulated CO as illustrated in Figures S3-S6. The resulting impact on O_3 isopleths is likely moderate because reducing CO would decrease the O_3 concentrations across the O_3 isopleths, but the patterns of the isopleths depicting the responses of O_3 to NO_X and VOC emissions would be likely retained.

The model also shows low biases in $PM_{2.5}$ (NMB= -32%) and PM_{10} (NMB= -51%), which could be associated with the exclusion of wind-blown dust emissions from the current simulation, a known underestimation in monoterpene SOA from oxidation in the aerosol scheme implemented in CMAQv5.0.2 (i.e., aero06), and the mechanistic simplifications on aging of primary and secondary organic aerosols, and photo-oxidation of intermediate volatility organic compounds.[69, 70] The underestimations in modeled PM may increase O_3 prediction through changing the photolysis rates and uptake of oxidants on aerosol surfaces.[71-74] Changing PM concentrations may change the modeled O_3 by similar levels across the O_3 isopleths, whereas the responses of O_3 to NO_X and VOCs should not be altered significantly.

Multiple CMAQ-HDDM simulations

We conduct CMAQ-HDDM simulations at 16 different NO_X and VOC emission levels (i.e., 1%, 50%, 100%, and 150% of NO_X by 1%, 50%, 100%, and 150% of VOCs). The 16 NO_X-VOC emission combinations correspond to 16 "vital points" on a O_3 isopleth diagram (Figure 1). The 16 vital points are selected as scattered as possible, and tried to be distributed evenly across the whole coordinational domain so that the integration-based and statistics-based interpolations could be of homogeneous power throughout the x-y and x-$\sqrt{y}$ plane. Any 0% points are not chosen because HDDM cannot calculate sensitivities for zero emission. It should be noted that although HDDM is more efficient for calculating sensitivities than the traditional "brute-force" mathematical approach, it is still computationally expensive. The average CPU time to achieve a one-day CMAQ-HDDM simulation with two first-order and three second-order sensitivity parameters is about 64,800 seconds (the CPUs are AMD Opteron(tm) Processor 6378, 2.4 GHz), though this could vary across hardware condition. The total CPU time of our simulation experiment (16 seven-month simulations) is about 2.2×10^8 seconds or 2,555 days.

Based on the model simulations, $C_{O3,pop}$ of a given region is calculated as follows:

$$C_{O_3,pop} = \frac{\sum_k POP_k \times C_{O_3,k}}{\sum_k POP_k} \quad \text{Eq. 6}$$

where subscript k denotes a model grid cell within the given region; $C_{O3,k}$ is the modeled O_3 concentration in grid cell k; POP_k is the total population in grid cell k. The population distribution within the study domain is derived from the LandScan dataset provided by Oak Ridge National Laboratory.[75] The LandScan 2017 version is used in this study to ensure a consistent base year with CMAQ-HDDM simulations. The spatial resolution of the population data is originally 30″ × 30″ (approximately 1 *km* on the equator) and is aggregated to get the same resolution of the model

domain (i.e., 36 *km*).

On the O_3 isopleth diagram, *x*-axis denotes the percentage of the total anthropogenic VOC emission, *y*-axis denotes the percentage of the total anthropogenic NO_X emission, and the isopleths represent the averaged $C_{O_3,pop}$ over the O_3 season. The 16 simulations provide $C_{O_3,pop}$ values together with their first-and second-order sensitivities at the 16 NO_X-by-VOCs emission vital points. In the *x*-*y* plane, the partial derivatives at the 16 vital points can be derived from HDDM sensitivities as follows,

$$\frac{\partial C_{O_3}}{\partial x}(x_i, y_i) = S_V(x_i, y_i) \cdot \frac{1}{x_i} \quad \text{Eq. 7}$$

$$\frac{\partial C_{O_3}}{\partial y}(x_i, y_i) = S_N(x_i, y_i) \cdot \frac{1}{y_i} \quad \text{Eq. 8}$$

$$\frac{\partial^2 C_{O_3}}{\partial x^2}(x_i, y_i) = S_{VV}(x_i, y_i) \cdot \frac{1}{x_i^2} \quad \text{Eq. 9}$$

$$\frac{\partial^2 C_{O_3}}{\partial y^2}(x_i, y_i) = S_{NN}(x_i, y_i) \cdot \frac{1}{y_i^2} \quad \text{Eq. 10}$$

$$\frac{\partial^2 C_{O_3}}{\partial x \partial y}(x_i, y_i) = S_{VN}(x_i, y_i) \cdot \frac{1}{x_i} \cdot \frac{1}{y_i} \quad \text{Eq. 11}$$

where subscript *i* denotes a specific vital point. *x* and *y* are coordinates of vital point *i*. The vital point (50%, 1%), for example, represents 50% emissions of VOCs and 1% emissions of NO_X. $S_V(x_i, y_i)$, $S_N(x_i, y_i)$, $S_{VV}(x_i, y_i)$, $S_{NN}(x_i, y_i)$, and $S_{VN}(x_i, y_i)$ are modeled sensitivities at vital point *i*. We generate the isopleths in the x-$\sqrt{y}$ plane (with the coordinates of *x* and square-root-transformed *y*) (Figure 1). In terms of Pearson's *r* and sum of squared residuals (SSRs), our tests show better performance when the isopleths are generated in this plane, compared to those generated in the original or logarithmic plane (Figure S8). The square-root association between NO_X and O_3 has been reported by a previous study based on semi-empirical analysis,[21] which partially explains the

better performance of the sensitivity-based integration in the x-$\sqrt{y}$ plane than in other planes. In the x-$\sqrt{y}$ plane, three of the five partial derivatives are different from those (Eq. 8, 10, and 11) in the original x-y plane. They are determined by the following equations that are derived from Eq. 7–11 using the chain rule, as

$$\frac{\partial C_{O_3}}{\partial y_t}(x_i, y_i) = S_N(x_i, y_i) \cdot \frac{2}{y_{ti}} \quad \text{Eq. 12}$$

$$\frac{\partial^2 C_{O_3}}{\partial y_t^2}(x_i, y_i) = S_{NN}(x_i, y_i) \cdot \frac{4}{y_{ti}^2} + S_N(x_i, y_i) \cdot \frac{2}{y_{ti}^2} \quad \text{Eq. 13}$$

$$\frac{\partial^2 C_{O_3}}{\partial x_t \partial y_t}(x_i, y_i) = S_{NV}(x_i, y_i) \cdot \frac{1}{x_{ti}} \cdot \frac{2}{y_{ti}} \quad \text{Eq. 14}$$

where x_t and y_t are the coordinates in the transformed x-$\sqrt{y}$ plane where $x_t = x$ and $y_t = \sqrt{y}$.

Method to derive O_3 isopleths

We develop a new method, high-order integration method (HIM), to combine multiple CMAQ-HDDM simulations. HIM starts from the mathematical integration of the second-order sensitivities including cross sensitivities, and then the first-order sensitivities, to finally generate the O_3 isopleths. In the x-$\sqrt{y}$ plane, the second-order partial derivatives of the 16 vital points are interpolated using the natural-neighbor interpolation method.[76] Based on the interpolated second-order derivatives, we conduct integration from the (100%, 100%) vital point to obtain the first-order derivatives on the 1:1 line (Figure 1). Then, from the 1:1 line along with both the horizontal and the vertical directions, we conduct the mathematical integration to fill the first-order derivatives at any point within the 0-150% emission range (Figure 1). The values of the first-order derivatives calculated by the horizontal and the vertical integration procedures can be slightly different from each other. They are averaged to get the calculated derivatives. It should be noted that except for starting from the vital point (100%, 100%) along the horizontal and vertical directions, it is viable to start from any vital

points along either path to complete the integration. To make sure that the calculated and modeled derivatives are identical at the 16 vital points, the residuals between the modeled and calculated derivatives are interpolated and added on top of the calculated layers to generate the first-order derivative plane, and the same procedures are applied to derive the corresponding O_3 concentrations under the transformed coordinate system from the generated first-order derivatives. We finally transform the coordinates from the x-$\sqrt{y}$ plane to the original x-y linear plane (Figure 1), whereby we obtain the final O_3 isopleths. This method maintains the continuity of the first- and second-order derivatives of an isopleth diagram and makes it feasible to make the full use of the differential information provided by multiple CMAQ-HDDM simulations.

In addition to HIM, we adopt alternative methods to derive the isopleths, including the first-order Integral Method (IM) where we only use the first-order sensitivities to generate the isopleths (i.e. DDM), the stepwise approach as proposed by previous studies,[45, 77] and the brute force approach where we directly interpolate the isopleth diagrams based on $C_{O_3,pop}$ values of the 16 vital points via nearest, linear, cubic, and natural-neighbor interpolation, respectively, without involving any sensitivities. The performance of HIM, IM, the stepwise approach, and the brute force approach are evaluated (see in RESULTS AND DISCUSSION). Note that the O_3 isopleths are derived by city, and the values of the isopleths are measured by the $C_{O_3,pop}$ of the city which is calculated as the population-weighted O_3-season-averaged MDA8h within the city. A total of 366 prefecture-level cities in China are considered in this study. The definition of prefecture-level cities in China contain both urban and rural regions under jurisdiction, in which sense urban-rural divergences of O_3 concentrations are not considered in this study.

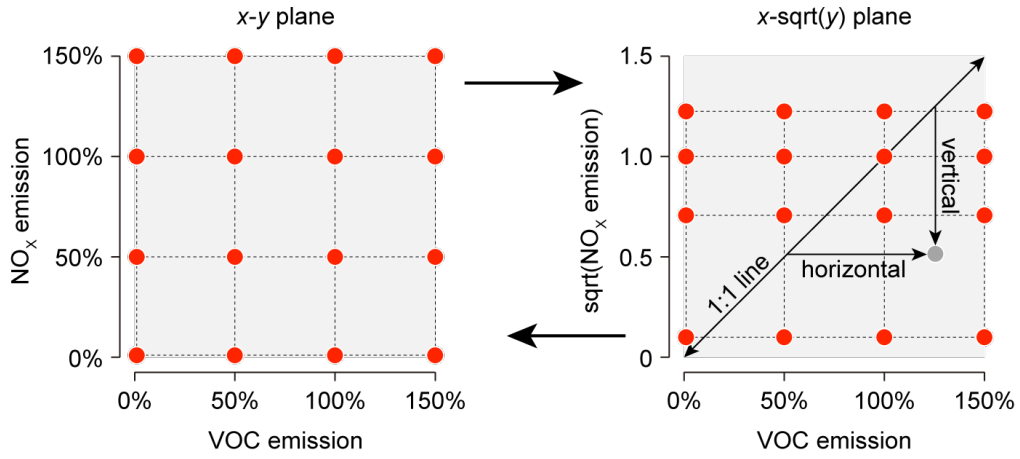

297

298 **Figure 1. Schematic of the coordinate system transformation and the High-order Integral**

299 **Method (HIM) to generate O_3 isopleths.** "sqrt" denotes square-root transformation.

300 **RESULTS AND DISCUSSION**

301 **Comparing the performance of different approaches**

302 The performance of the four approaches to generating O_3 isopleth diagrams (i.e., HIM, IM, the
303 stepwise approach, and the brute-force approach) is evaluated for each city by randomly selecting
304 15 of the 16 vital points to draw the isopleth diagram with the one remaining point for validation.
305 The $C_{O3,pop}$ calculated by the four methods at the remaining vital point are plotted against the $C_{O3,pop}$
306 directly modeled by CMAQ in Figure 2 along with *r* and SSR. The $C_{O3,pop}$ calculated by the four
307 methods are all significantly correlated with the CMAQ-modeled $C_{O3,pop}$ at the significance level of
308 0.01. Among these methods, HIM, IM, and the stepwise approach are of the *r* values quite close to
309 1, but the SSR of HIM is over an order of magnitude lower than the SSR of IM and nearly two
310 orders of magnitude lower than the SSR of the stepwise approach (Figure 2), suggesting better
311 performance of HIM than IM and stepwise. IM is biased high at high levels of $C_{O3,pop}$ (Figure 2),
312 while the stepwise approach is biased high at low levels of $C_{O3,pop}$. The linear interpolation is chosen
313 as a representative of the brute force approach. The performances of other interpolation methods,

including the cubic, natural-neighbor, and nearest interpolations, implemented in the brute-force approach are shown in Figure S9, which performed similarly to each other in terms of *r* values (0.49–0.50) and SSRs (2.3×10^5–2.4×10^5). All these three methods are severely lowly biased and thus inferior to HIM and IM. The low biases are more pronounced at the four 50% NO_X-associated vital points as (1%, 50%), (50%, 50%), (100%, 50%), and (150%, 50%), suggesting that O_3 levels would be underestimated by the brute-force approach as NO_X emissions further decline – an expectable trend in China. Due to the limitation of these interpolation methods, $C_{O3,pop}$ at the vital points of (1%, 1%), (150%, 1%), (150%, 1%), and (150%, 150%) cannot be extrapolated and are set to null (Figure 2, resulting in the cycles falling on the *x*-axis). The nearest interpolation method shows the lowest *r* value ($r = 0.20$, SSR = 87680.9) with large biases especially at low $C_{O3,pop}$ levels (Figure S9). Overall, HIM has the best performance ($r = 1.00$, SSR = 89.6) in generating the O_3 isopleth diagrams among the existing approaches.

We also compare the isopleths derived from the 16 vital points with the isopleths derived from one single specific vital point: (100%, 100%). Taking Beijing as an example, the isopleths generated by the single vital point highly resemble the isopleths generated from the 16 vital points (mostly with a difference of <5%) when the changes in NO_X and VOC emissions are within -60%–40% (Figure S10). This similarity confirms that CMAQ-HDDM is an efficient tool for sensitivity analysis, coinciding with results from Hakami et al.[39] as the O_3 isopleths constructed from multi-order sensitivities by mathematical integrations having well reproduced the mechanism-driven model predictions have justified the credibility of the estimated sensitivities from side. Relatively large differences are found when the NO_X emission is reduced by more than 70%, where the O_3 photochemistry falls deep into the NO_X-sensitive regime (Figure S10), and $C_{O3,pop}$ is biased by more

than 10%. To better reproduce the O_3 changes to a wide range of emission changes, we use information of all the 16 vital points to generate isopleths and conduct subsequent assessments.

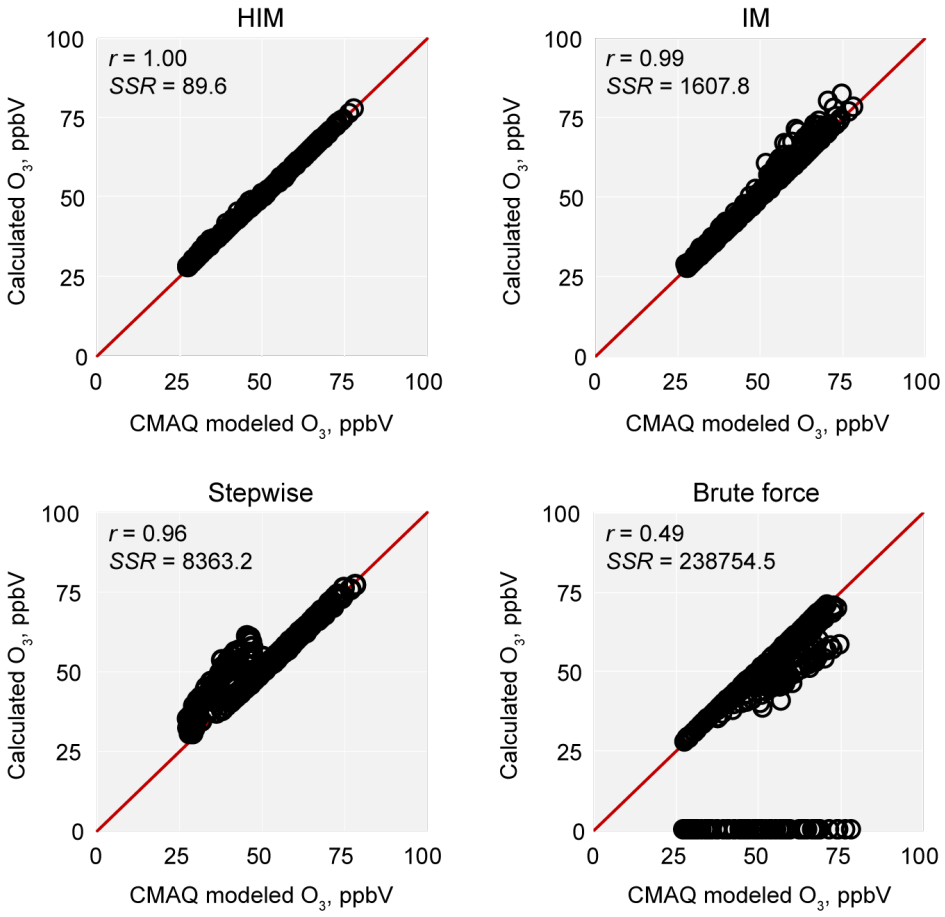

Figure 2. Evaluation of the performance of different methods to generate O_3 isopleths. The methods include HIM, IM, the stepwise approach, and the brute force approach. Linear interpolation is used in the brute force approach. Figure S9 shows the performance of the brute force approach using other interpolation methods, including nearest, cubic, and natural-neighbor interpolation. The performance is evaluated by randomly selecting 15 out of 16 vital points to generate the isopleths for each city. The remaining one (labelled as "CMAQ modelled O_3") is compared with that calculated using the isopleths ("Calculated O_3"), as shown in the figure where each circle represents a city. The red solid line is the 1:1 line. The Pearson's correlation coefficient

348 (r) and the sum of squared residuals (SSRs) are noted in each panel.

349

350 **National-level O_3 isopleths, historical and future trajectories**

351 The average of the modeled O_3 concentrations at monitoring sites is 55 ppbV during the O_3 season,
352 in line with observations (57 ppbV). Most of the sites are located in urban areas and thus less
353 representative for rural population. In order to cover the entire population, we use model results to
354 calculate $C_{O_3,pop}$. Our simulation shows that the average O_3-season $C_{O_3,pop}$ in China in 2017 is 59
355 ppbV. 95% of the population are being exposed to ambient O_3 at levels between 44 and 71 ppbV.
356 100% and 97% of the population reside in places that have at least one day in 2017 exceeding the
357 Chinese Level-I and II health-based Ambient Air Quality Standards for MDA8h O_3, respectively
358 (the Level-I and II standards are 50.9 and 81.5 ppbV, respectively, note that the official standards
359 are defined in $\mu g \cdot m^{-3}$ under a reference condition as 100 and 160 $\mu g \cdot m^{-3}$ and converted here to
360 ppbV).[78, 79] If measured by the United States O_3 standard which is 70 ppbV for the annual fourth-
361 highest MDA8h O_3,[11] 99% of the Chinese population live in non-attainment areas, compared to 30%
362 in the United States in the same year,[29, 80] suggesting severe O_3 pollution in China.
363 We generate the isopleths of national-level $C_{O_3,pop}$ using HIM (Figure 3a). The national-level
364 isopleths depict overall responses of O_3 exposure of the entire Chinese population to emission
365 controls. Given that the O_3 exposure of the entire population is directly associated with the health
366 burden of the country from O_3 pollution, the national-level isopleths have important political and
367 health implications. On the isopleths, we add the $S_N=S_V$ and $S_N=0$ lines (Figure 3a). The $S_N=S_V$ line
368 divides the diagram into two major regimes: above this line is the VOC-limited regime where VOC
369 reduction is more effective for reducing O_3; below this line is the NO_X-limited regime where NO_X

reduction is more effective.[14] Above the S_N=0 line outlines the NO_X-saturated regime – a part of the VOC-limited regime, where NO_X reduction increases O_3 (Figure 3a). In addition, we define the transition regime when the ratio of S_N to S_V lies between 0.8 and 1.2, where reductions in NO_X and VOCs are almost equally beneficial (Figure 3a, the shaded area around the S_N=S_V line). The sensitivities of $C_{O_3,pop}$ to NO_X and VOC emissions show an overall VOC-limited regime in China (S_N = 2.4 ppbV, S_V = 5.3 ppbV, S_N/S_V = 0.45) (Table S1), suggesting that the VOC reduction is more effective for O_3 mitigation, though both NO_X and VOC reductions are beneficial.

The second-order sensitivities of S_{NN}, S_{VV}, and S_{NV} are -12.0, -3.1, and 5.0 ppbV, respectively (Table S1). Negative S_{NN} and S_{VV} reflect an increase in S_N and S_V as the emissions decline. The higher absolute value of S_{NN} than that of S_{VV} ($|S_{NN}|$ = 12.0, $|S_{VV}|$ = 3.1) suggests a faster increase in S_N as the NO_X emission decreases than in S_V as the VOC emission decreases by the same percentage. Therefore, although VOC reduction is currently more effective for O_3 mitigation, NO_X reduction could become more and more effective as emissions continuously decrease and have the larger potential for O_3 mitigation than VOC reduction. This tendency is well confirmed by the O_3 isopleths (Figure 3a) which show a reduction of 4.3 ppbV in $C_{O_3,pop}$ due to a 50% reduction in NO_X, 28% larger than the $C_{O_3,pop}$ reduction achieved by a 50% reduction in VOCs (3.3 ppbV). The corresponding S_N (16.3 ppbV) at (100%, 50%) is 135% larger than the S_V (6.9 ppbV) at (50%, 100%). Unlike the S_{NN} and S_{VV}, the cross sensitivity S_{NV} (5.0 ppbV) is positive, indicating that reducing either NO_X or VOCs would cause the other one being less effective for O_3 abatement (due to a decrease in the first-order sensitivity). For example, the S_V decreases from 5.3 to 2.2 ppbV when reducing the NO_X emission by 50%, and similarly, the S_N decreases from 2.4 to 0.2 ppbV when reducing the VOC emission by 50%. As a result, although simultaneously reducing both NO_X and

VOC emissions would achieve a larger $C_{O_3,pop}$ reduction (5.9 ppbV) than solely reducing either NO_X (4.3 ppbV) or VOCs (3.3 ppbV), the $C_{O_3,pop}$ reduction of the former would be 23% smaller than the sum of the latter two. The first- and second-order sensitivities and O_3 concentrations of the national average $C_{O_3,pop}$ at the 16 vital points are summarized in Table S1.

It has been reported that the total anthropogenic NO_X emissions in China continuously increased between 1970 and 2012 from 12 $Tg \cdot yr^{-1}$ to 29 $Tg \cdot yr^{-1}$ and then decreased by about one quarter between 2012 and 2017, and that VOC emissions kept increasing throughout the entire period, although gradually levelled off after 2012 (Figure 3 and S11).[81] Corresponding to the reported historical emission trajectories, the overall $C_{O_3,pop}$ in the isopleths started from the NO_X-limited regime in 1970, switched to the VOC-limited regime in around 2004, and stayed in the VOC-regime through 2017 (Figure 3a). The combination of the emission trajectories and the shift in O_3 regimes results in a generally increasing trend in $C_{O_3,pop}$ since 1970 which peaks in 2014 and then slightly declined in the most recent years (Figure 3b). Note that the $C_{O_3,pop}$ trend in Figure 3b only shows the response of O_3 to changing NO_X and VOC emissions, while other factors, such as climate conditions and emissions of other compounds, are assumed unchanged as in 2017. The trend, therefore, cannot be regarded as a historical reconstruction of $C_{O_3,pop}$.

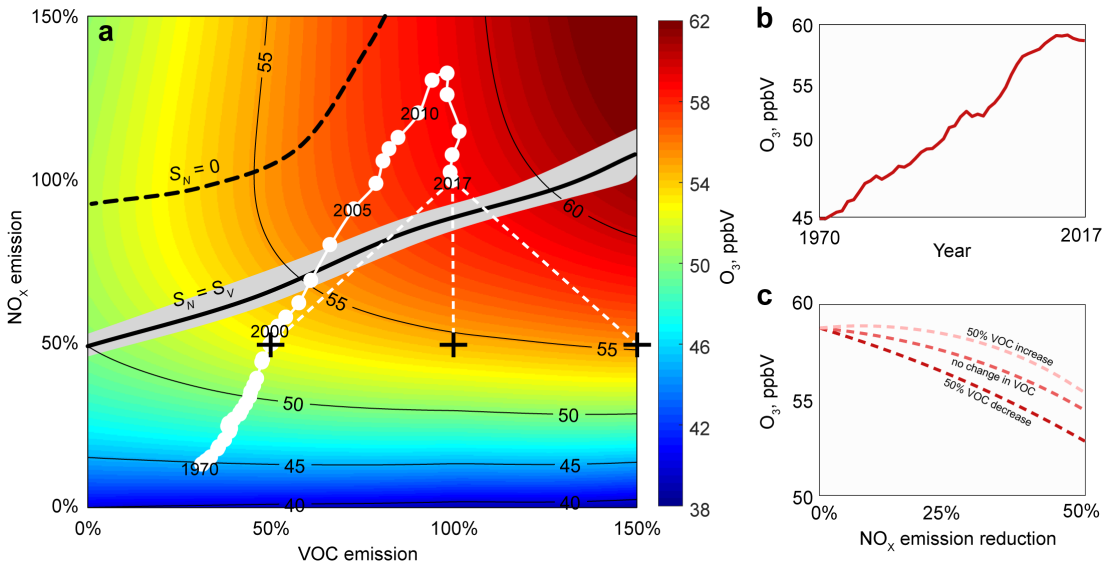

Figure 3. The O_3 isopleths and the historical and future trends of O_3 in China. a. The O_3 isopleths in China showing the responses of the O_3 concentration to the changes in total anthropogenic emissions of NO_X and VOCs. O_3 concentrations are calculated as the population-weighted average O_3-season MDA8h O_3 across China. The S_N=0 line, the S_N=S_V line, the historical emission trajectory since 1970, and the three VOC emission reduction scenarios are marked in the isopleth diagrams by the black dashed line, the solid line, the white circles, and the white dashed line, respectively. The shaded area represents the transition regime. **b.** The O_3 concentrations in response to the historical NO_X and VOC emissions during 1970–2017 derived from the O_3 isopleths. This O_3 trend corresponds to the black solid line in panel a. **c.** The future trends of O_3 concentrations under different emission reduction scenarios. The historical trends of NO_X and VOC emissions are derived from the Multi-resolution Emission Inventory for China version 1.2.[81] The scenario projections are realized by prescribing +50%, no change, and -50% change of VOC emissions, crossed with 0–50% reduction of NO_X. Note that Figure 3 illustrates the overall response of $C_{O_3,pop}$ to precursors emissions in China, but different regions have different levels of NO_X and VOC emissions and may represent different responses.

To show how the future O_3 trends would differ by different emission reduction strategies, we design three emission scenarios in which NO_X emissions are consistently reduced by 50% while VOC emissions either increase by 50%, or remain constant, or decrease by 50% (marked as white dashed lines in Figure 3a). Notably, an 1-ppbV decrease in the national average $C_{O_3,pop}$ would avoid approximately 5,300 deaths per year from exposure to ambient O_3, indicating marked health benefits from O_3 mitigation (Section S3 in the Supporting Information). Under the increasing-VOC scenario, the $C_{O_3,pop}$ would eventually decrease by 3.4 ppbV but would change little with the first 25% NO_X reduction; under the constant-VOC and decreasing-VOC scenarios, the $C_{O_3,pop}$ would show a gradual decrease of 4.3 and 5.9 ppbV, respectively (Figure 3c). The different $C_{O_3,pop}$ values at the end of the three scenarios demonstrate an important role of VOC reduction in O_3 mitigation despite that reducing NO_X is more efficient. When zeroing out the anthropogenic NO_X and VOC emissions, the isopleths imply a background $C_{O_3,pop}$ of ~40 ppbV (Figure 3a).

O_3 isopleths for individual cities

The national-level analysis demonstrates the population-weighted O_3 concentration of the country to historical and future emission changes, but different cities may respond differently, as reflected by the different patterns of the city-specific O_3 isopleths in Figure 4. Different cities respond differently to NO_X and VOC emission changes, as reflected by the different patterns of their O_3 isopleths. Figure 4 illustrates the O_3 isopleths for six representative cities. Beijing and Guangzhou are two of the most developed cities in China, with populations of 21 and 13 million, respectively.[82-84] As marked by the black crosses on the city-specific O_3 isopleths, $C_{O_3,pop}$ in these two cities are currently in the NO_X-saturated regime, and thus, reducing VOCs is effective for O_3 mitigation in

447 these cities, while reducing NO_X increases O_3. Chengdu, an inland capital city and a megacity with
448 a population of ~14 million,[84, 85] also shows a NO_X-saturated O_3 regime, but the NO_X titration effect,
449 quantified by the magnitude of the increase in ambient O_3 in response to a decrease in ambient NO_X,
450 in Chengdu is weaker than in Beijing and Guangzhou as indicated by S_N, that -7.4, -15.5, and -4.0
451 ppbV in Beijing, Guangzhou, and Chengdu, respectively. Moderately or less developed cities are
452 more divided in their O_3 isopleths patterns, but their current $C_{O_3,pop}$ locations in O_3 isopleths are
453 generally close to or below the S_N=S_V line (e.g., Jiaozuo, Changsha, and Yuxi in Figure 4). Yuxi in
454 Yunnan province (Figure 4), as a representative less-developed city, falls deep into the NO_X-limited
455 regime (S_N and S_V are 6.2 and 0.5 ppbV, respectively) and shows a relatively low level of ambient
456 O_3 (46.0 ppbV).
457 Generally, the city-specific O_3 isopleths provide intuitive perceptions on the local surface O_3 control
458 strategies. Taking Beijing as an example, the annual average surface O_3 concentration in 2017 was
459 67.5 ppbV (i.e. the 100% NO_X and VOC emissions in the isopleth). Reducing the NO_X emission
460 down to 50% while keeping the VOC emission constant could decrease the O_3 to 66.4 ppbV, and
461 reducing the VOC emission to 50% while holding the NO_X emission as the same could control the
462 O_3 to 59.5 ppbV, indicating emissions of VOCs should be restricted in priority for Beijing at the
463 current status. The background O_3 concentration, defined at the (0%, 0%) emission coordination,
464 could reflect the O_3 pollution abatement potential under the zero-emission ideal circumstances (as
465 45.0 for Beijing). However, elimination of all NO_X and VOC emissions are never pragmatic, and
466 hence setting the Level-I standard (50.4 ppbV) as our policy target would be more feasible, which
467 could be achieved by suppressing the NO_X emissions strictly to lower than 10% of the current
468 condition, where VOC emissions would be of limited effects. The paradox that we should first lower

down the VOCs to alleviate the high O_3 pollutions but radically we have to restrict the NO_X to a rather low level to control the O_3 for Beijing in the long-run, shall be the most valuable realistic implication at the policy level, which could arouse future researches in cost-effective analyses and policy-making.

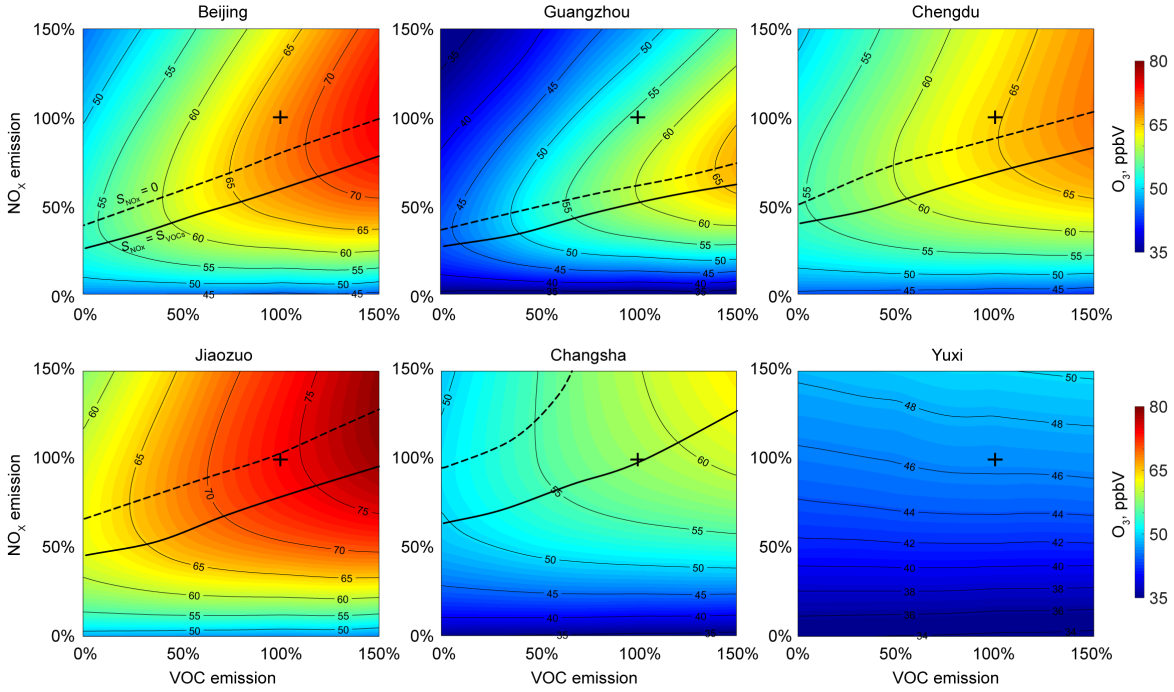

Figure 4. O_3 isopleths for six representative cities. The black cross marks the $C_{O_3,pop}$ under 100% of NO_X and VOC emissions, i.e., the current positions (2017) on the isopleths. The black dashed line is where the sensitivity to NO_X emission changes is zero (above which, increased NO_X emissions decrease O_3), and the solid black line is where the VOC and NO_X emission sensitivities are the same.

Spatial distribution

Figure 5 shows the spatial distributions of S_N, S_V, and $C_{O_3,pop}$ covering the 366 cities in China. 34% of the cities, where 48% of the Chinese population reside, are in the VOC-limited regime. 14% of

484 the cities, where 25% of the Chinese population reside, show negative S_N (Figure 5a) and therefore,
485 are classified into the NO_X-saturated regime. These cities in the NO_X-saturated regime often have
486 high S_V (Figure 5b). Cities in the VOC-limited regime are mostly located in the eastern China
487 (Figure 5c). Those in the NO_X-saturated regime are clustered in four major regions, as the North
488 China Plain (NCP), Yangtze River Delta (YRD), Pearl River Delta (PRD), and Northeast China
489 (Figure 5a). In particular, the first three regions are the target regions of several landmarks for
490 tackling air pollution in China.[46, 86] Our results indicate that the stringent control over NO_X
491 emissions is expected to cause a continuous increase in O_3 in these regions likely due to reduced
492 NO_X titration.[87, 88] The negative S_N in Northeast China, particularly in Liaoning, might be
493 attributable to high local emissions from heavy industries and a cold climate which have favored
494 the pollutants accumulation due to the cool air stagnation effect.[89-92] The majority of the cities in the
495 middle and western parts are in the NO_X-limited regime with relatively high S_N and low S_V. A
496 complete list of the city-specific first- and second-order sensitivities are provided in Supplemental
497 Dataset. The correlation between S_N and S_V of individual cities is significant ($p\text{-}value = 10^{-43}$) (Figure
498 S12). It is noteworthy that there are strong correlations between S_V and the three second-order
499 sensitivities (Figure S12). These correlations may facilitate a quick estimation by regression-based
500 approximation for the second-order sensitivities from S_V, as direct generation of them from CMAQ
501 models could be rather computational costly.
502 We collect observation data based on a thorough literature review and compare the observation-
503 based O_3 regimes with the simulation results (Table S2). Given the rapid change in the severity of
504 O_3 pollution in recent years in China, we only consider the most recent measurements, i.e., those
505 conducted in 2015 and beyond. Measurements are concentrated in NCP, YRD, and PRD, with a

limited number of measurements conducted outside these three regions (Table S2). In line with our simulation, most measurements reveal a VOC-limited regime in these three regions. For example, both the observations and the simulation fall in VOC-limited regimes at the six sites in three NCP cities as Beijing, Tianjin, Zhengzhou (Table S2), other than which a relatively larger disagreement is detected (Table S2), probably due to the mismatch in time – the measurements showing disagreement in other regions were all conducted before 2017, which was the baseline year of our simulation. Overall, the simulation results match the observed O_3 regimes at 20 out of the 33 sites (Table S2), suggesting fair performance of the model.

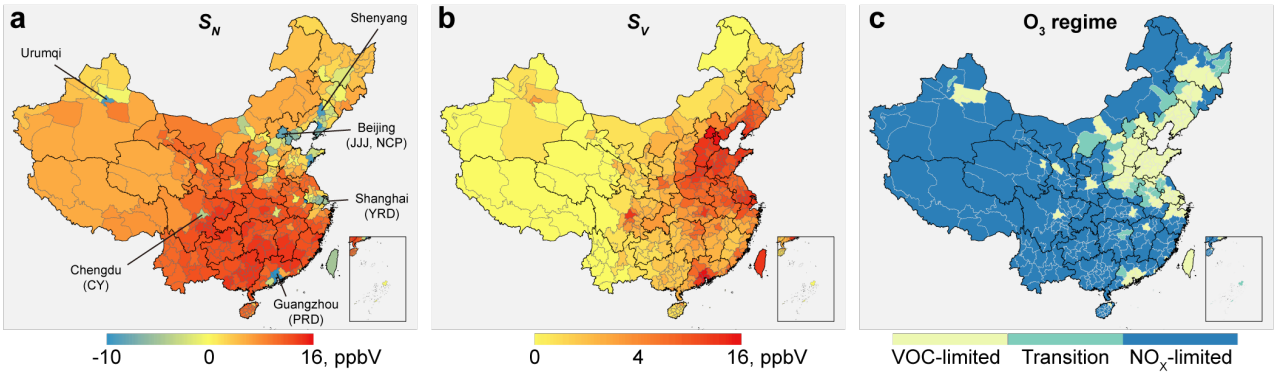

Figure 5. The spatial patterns of the city-level S_N (a), S_V (b), and O_3 regimes (c). S_N and S_V are the modeled sensitivities of O_3 concentrations to anthropogenic NO_X and VOC emissions, respectively, and are represented by the O_3 concentration change due to a 100% change in NO_X and VOC emissions, respectively. The O_3 regime for each city is determined by the ratio of S_N to S_V (NO_X-limited if $S_N/S_V > 1.2$, transitioning if $0.8 < S_N/S_V \leq 1.2$, VOC-limited otherwise). Several representative cities are marked with the regions where the cities are located: Jing-Jin-Ji (JJJ), Yangtze River Delta (YRD), Pearl River Delta (PRD), and Cheng-Yu (CY) (Figure 5a).

Temporal trends

We further investigate the temporal trends in $C_{O_3,pop}$, S_N, and S_V in China with a focus on four representative regions, as the Jing-Jin-Ji metropolitan area (JJJ, located in the north of NCP), YRD, PRD, and the Cheng-Yu metropolitan area (CY, an inland metropolitan area circumscribing Chengdu and Chongqing, alternatively named as "Yu", in the southwest China). Temporally, $C_{O_3,pop}$ across China peaks in May (Figure 6), in accordance with ground-level observations in 2017 (Figure S13), which is likely affected by long-range transport and intrusion from the stratosphere.[93-95] Similar peaks in May were also evident in YRD, PRD, and CY (Figure 6). Both modeled $C_{O_3,pop}$ and observed O_3 concentrations exhibit multiple peaks over PRD (for example, in May and September-October) (Figures 6 and S5). Note that due to recent emission control and climate variation, the intra-annual temporal patterns of $C_{O_3,pop}$ may vary by year (Figure S13). S_N summit in June-July-August across all China regions except PRD which exhibits multiple peaks. S_V, on the other hand, shows a trough in summer in most regions, which shall be attributed to the strong solar radiations in summer that endow the photolysis of NO_X with predominant position over the contribution from VOCs, so that the O_3 sensitivities from VOCs were suppressed. The ratio of S_N to S_V generally peaks in summer, suggesting that a NO_X-limited regime is of higher frequency to occur in summer; while an exception is PRD where S_N/S_V ratios are mostly negative throughout the study period. Large variability of the ratios is evident within each region as illustrated by the shaded areas in Figure 6 (see Section S4 in the Supporting Information for detailed discussion on relationships between sensitivity coefficients and climate variables).

We find that compared to the 10% of days with lowest O_3 in each region, the 10% of days with higher O_3 are often concurrent with higher levels of S_N, S_V, and S_N/S_V ratios (Figure S14). On the

546 low-O_3 days, S_N are more inclined to be negative, suggesting a stronger NO_X titration effect. The
547 policy implication from our results is that reducing NO_X emissions are more efficient for controlling
548 O_3 on high O_3 pollution episodes towards the prescribed O_3 standards, but less effective on low-O_3
549 days. Taking JJJ as an example, the highest O_3 pollution occurred on June 30, 2017 as 148.1 ppbV,
550 when S_N was 24.8 ppbV, indicating that surface O_3 pollution could be alleviated by 0.248 ppbV per
551 1% NO_X emission reduction. However, for the median O_3 pollution days like September 2, 2017
552 when the O_3 concentration was close to 70 ppbV, S_N was modeled to be 7.1 ppbV, which corresponds
553 to 0.071 ppbV O_3 reduction per 1% NO_X emission reduction, showing lower effects from NO_X
554 emission control. As for the lowest O_3 concentration on October 22, 2017 as 28.0 ppbV, the S_N was
555 -13.6 ppbV, suggesting that surface O_3 pollution could even be elevated by 0.136 ppbV when
556 reducing 1% NO_X emission. Solely reducing NO_X may increase O_3 on the low-O_3 days, which has
557 also been verified during the COVID-19 quarantine in winter 2020 when O_3 was significantly
558 elevated across China in response to the quarantine-induced reduction in NO_X emissions.[96]
559

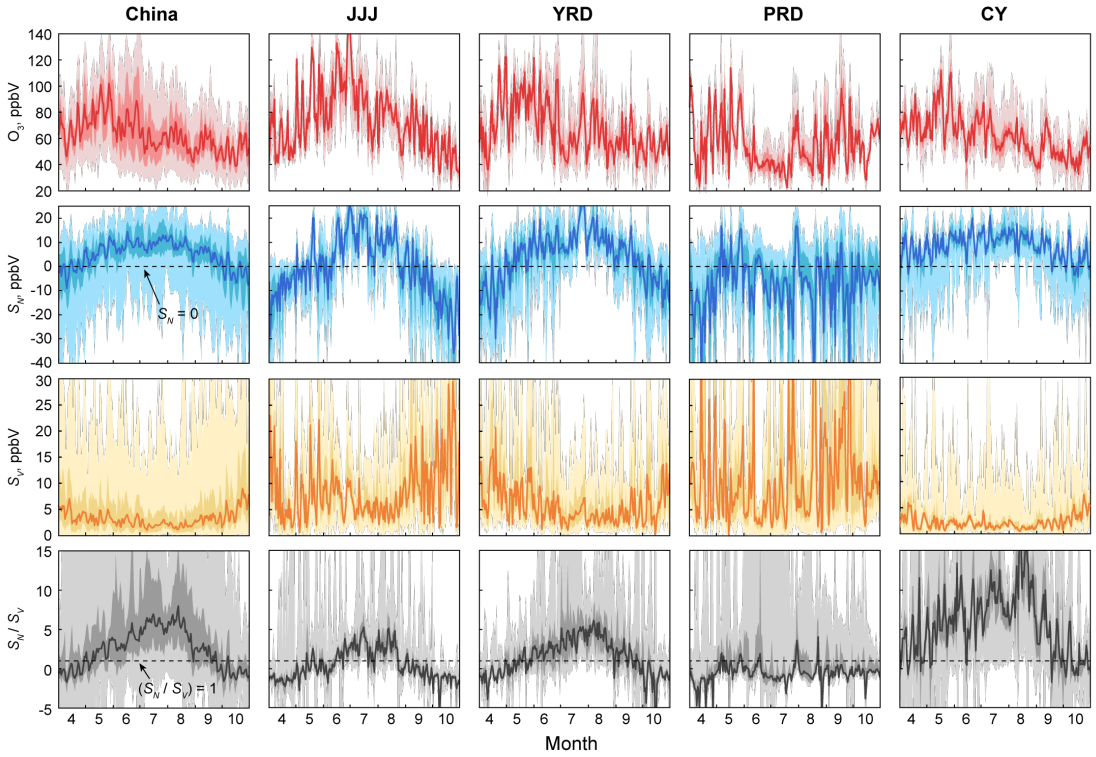

Figure 6. Daily variations in MDA8h O_3 concentrations, S_N, S_V, and S_N/S_V in China and four target regions during the O_3 season in 2017. The four regions are Jing-Jin-Ji (JJJ), Yangtze River Delta (YRD), Pearl River Delta (PRD), and Cheng-Yu (CY) (Figure 5a). Variables are shown as population weighted levels in the regions. In each panel, the solid line indicates the median level; the shaded area with the dark color presents the inter-quartile range covering 50% population; the shaded area with the light color denotes the 95% interval.

Supporting Information. Further detailed illustrations on treatment of HONO emission and chemistry in the model (S1), VOC speciation in CB05 mechanism (S2), methodologies for health assessment (S3) and detailed discussion on relationships between sensitivity coefficients and climate features (S4). A total of 14 supplementary figures and 2 tables.

ACKNOWLEDGMENTS

This research is supported by the U.S. Environmental Protection Agency (EPA grant number R835880), the U.S. National Science Foundation (NSF SRN grant number 1444745), and the National Natural Science Foundation of China (Grant 41991310). Its contents are solely the responsibility of the grantee and do not necessarily represent the official views of the supporting agencies. Furthermore, the U.S. and China government does not endorse the purchase of any commercial products or services mentioned in the publication.

References

1. United States Environmental Protection Agency *Air Quality Criteria for Ozone and Related Photochemical Oxidants*; EPA 600/R-05/004aF; 2006.
2. Turner, M. C.; Jerrett, M.; Pope III, C. A.; Krewski, D.; Gapstur, S. M.; Diver, W. R.; Beckerman, B. S.; Marshall, J. D.; Su, J.; Crouse, D. L., Long-term ozone exposure and mortality in a large prospective study. *Am J Respir Crit Care Med* **2016,** *193*, (10), 1134-1142.
3. Bell, M. L.; McDermott, A.; Zeger, S. L.; Samet, J. M.; Dominici, F., Ozone and short-term mortality in 95 US urban communities, 1987-2000. *JAMA* **2004,** *292*, (19), 2372-2378.
4. Monks, P. S.; Archibald, A.; Colette, A.; Cooper, O.; Coyle, M.; Derwent, R.; Fowler, D.; Granier, C.; Law, K. S.; Mills, G., Tropospheric ozone and its precursors from the urban to the global scale from air quality to short-lived climate forcer. **2015,** *15*, 8889-8973.
5. Wang, T.; Xue, L.; Brimblecombe, P.; Lam, Y. F.; Li, L.; Zhang, L., Ozone pollution in China: A review of concentrations, meteorological influences, chemical precursors, and effects. *Sci Total Environ* **2017,** *575*, 1582-1596.
6. IHME Institute for Health Metrics and Evaluation (IHME). GBD Compare; Seattle, WA: IHME, University of Washington. <http://vizhub.healthdata.org/gbd-compare>. (*accessed on* 01/14/2020).
7. Li, K.; Jacob, D. J.; Liao, H.; Shen, L.; Zhang, Q.; Bates, K. H., Anthropogenic drivers of 2013–2017 trends in summer surface ozone in China. *Proceedings of the National Academy of Sciences* **2019,** *116*, (2), 422-427.
8. Shen, L.; Jacob, D. J.; Liu, X.; Huang, G.; Li, K.; Liao, H.; Wang, T., An evaluation of the ability of the Ozone Monitoring Instrument (OMI) to observe boundary layer ozone pollution across China: application to 2005–2017 ozone trends. *Atmospheric Chemistry and Physics* **2019,** *19*, (9), 6551-6560.
9. Ma, Z.; Xu, J.; Quan, W.; Zhang, Z.; Lin, W.; Xu, X., Significant increase of surface ozone at a rural site, north of eastern China. *Atmospheric Chemistry and Physics* **2016,** *16*, (6), 3969-3977.
10. Sun, L.; Xue, L.; Wang, T.; Gao, J.; Ding, A.; Cooper, O. R.; Lin, M.; Xu, P.; Wang, Z.; Wang, X., Significant increase of summertime ozone at Mount Tai in Central Eastern China. *Atmospheric Chemistry and Physics* **2016,** *16*, (16), 10637-10650.
11. United States Environmental Protection Agency, National Ambient Air Quality Standards for Ozone. In *Rules and Regulations*, Federal Register, 2015; Vol. 40 CFR Parts 50, 51, 52, 53, and 58.
12. Crippa, M.; Janssens-Maenhout, G.; Dentener, F.; Guizzardi, D.; Sindelarova, K.; Muntean, M.; Van Dingenen, R.; Granier, C., Forty years of improvements in European air quality: regional policy-industry interactions with global impacts. *Atmospheric Chemistry and Physics* **2016,** *16*, (6), 3825-3841.
13. Cohan, D. S.; Hakami, A.; Hu, Y.; Russell, A. G., Nonlinear response of ozone to emissions: source apportionment and sensitivity analysis. *Environ. Sci. Technol.* **2005,** *39*, 6739-48.
14. Sillman, S., The relation between ozone, NO*x* and hydrocarbons in urban and polluted rural environments. *Atmos. Environ.* **1999,** *33*, (12), 1821-1845.
15. Tonse, S. R.; Brown, N. J.; Harley, R. A.; Jin, L., A process-analysis based study of the ozone weekend effect. *Atmos Environ* **2008,** *42*, (33), 7728-7736.
16. Seinfeld, J. H.; Pandis, S. N., *Atmospheric chemistry and physics: from air pollution to climate change*. John Wiley & Sons: 2016.
17. Chameides, W. L.; Fehsenfeld, F.; Rodgers, M. O.; Cardelino, C.; Martinez, J.; Parrish, D.; Lonneman, W.; Lawson, D. R.; Rasmussen, R. a.; Zimmerman, P.; Greenberg, J.; Mlddleton, P.; Wang, T., Ozone precursor relationships in the ambient atmosphere. *J Geophys Res* **1992,** *97*, 6037.
18. Kinosian, J. R., Ozone-precursor relationships from EKMA diagrams. *Environ. Sci. Technol.* **1982,** *16*, (12), 880-883.
19. Seinfeld, J. H., Urban air pollution: state of the science. *Science* **1989,** *243*, (4892), 745-752.
20. Council, N. R., *Rethinking the ozone problem in urban and regional air pollution*. National Academies Press: 1992.
21. Chang, T. Y.; Rudy, S. J., Ozone-precursor relationships: a modeling study of semiempirical relationships. *Environ Sci Technol* **1993,** *27*, (10), 2213-2219.
22. Qian, Y.; Henneman, L. R.; Mulholland, J. A.; Russell, A. G., Empirical Development of Ozone Isopleths: Applications to Los Angeles. *Environmental Science & Technology Letters* **2019,** *6*, (5), 294-299.
23. Milford, J. B.; Russell, A. G.; McRae, G. J., A new approach to photochemical pollution control: Implications of spatial patterns in pollutant responses to reductions in nitrogen oxides and reactive organic gas emissions. *Environ Sci Technol* **1989,** *23*, (10), 1290-1301.
24. Pusede, S.; Cohen, R., On the observed response of ozone to NO*x* and VOC reactivity reductions in San Joaquin Valley California 1995–present. *Atmospheric Chemistry and Physics* **2012,** *12*, (18), 8323-8339.

25. Baidar, S.; Hardesty, R.; Kim, S. W.; Langford, A.; Oetjen, H.; Senff, C.; Trainer, M.; Volkamer, R., Weakening of the weekend ozone effect over California's South Coast Air Basin. *Geophys Res Lett* **2015,** *42*, (21), 9457-9464.
26. Reynolds, S. D.; Blanchard, C. L.; Ziman, S. D., Understanding the effectiveness of precursor reductions in lowering 8-Hr ozone concentrations Part II. The eastern United States. *J Air Waste Manag Assoc* **2004,** *54*, (11), 1452-1470.
27. Sierra, A.; Vanoye, A.; Mendoza, A., Ozone sensitivity to its precursor emissions in northeastern Mexico for a summer air pollution episode. *J Air Waste Manag Assoc* **2013,** *63*, (10), 1221-1233.
28. Hakami, A.; Odman, M. T.; Russell, A. G., Nonlinearity in atmospheric response: A direct sensitivity analysis approach. *Journal of Geophysical Research: Atmospheres* **2004,** *109*, (D15), 303.
29. Shen, H.; Chen, Y.; Li, Y.; Russell, A. G.; Hu, Y.; Henneman, L. R.; Odman, M. T.; Shih, J.-S.; Burtraw, D.; Shao, S., Relaxing energy policies coupled with climate change will significantly undermine efforts to attain us ozone standards. *One Earth* **2019,** *1*, (2), 229-239.
30. Xing, J.; Ding, D.; Wang, S.; Dong, Z.; Kelly, J. T.; Jang, C.; Zhu, Y.; Hao, J., Development and application of observable response indicators for design of an effective ozone and fine-particle pollution control strategy in China. *Atmospheric Chemistry and Physics* **2019,** *19*, (21), 13627-13646.
31. Guo, H.; Chen, K.; Wang, P.; Hu, J.; Ying, Q.; Gao, A.; Zhang, H., Simulation of summer ozone and its sensitivity to emission changes in China. *Atmospheric Pollution Research* **2019,** *10*, (5), 1543-1552.
32. Xing, J.; Wang, S.; Jang, C.; Zhu, Y.; Hao, J., Nonlinear response of ozone to precursor emission changes in China: a modeling study using response surface methodology. *Atmospheric Chemistry and Physics* **2011,** *11*, (10), 5027.
33. Ashok, A.; Barrett, S. R. H., Adjoint-based computation of U.S. nationwide ozone exposure isopleths. *Atmos Environ* **2016,** *133*, 68-80.
34. Xing, J.; Wang, S.; Zhao, B.; Wu, W.; Ding, D.; Jang, C.; Zhu, Y.; Chang, X.; Wang, J.; Zhang, F.; Hao, J., Quantifying Nonlinear Multiregional Contributions to Ozone and Fine Particles Using an Updated Response Surface Modeling Technique. *Environ Sci Technol* **2017,** *51*, (20), 11788-11798.
35. Xu, J.; Tie, X.; Gao, W.; Lin, Y.; Fu, Q., Measurement and model analyses of the ozone variation during 2006 to 2015 and its response to emission change in megacity Shanghai, China. *Atmos Chem Phys* **2019,** *19*, (14), 9017-9035.
36. Hakami, A.; Henze, D. K.; Seinfeld, J. H.; Singh, K.; Sandu, A.; Kim, S.; Byun, D.; Li, Q., The adjoint of CMAQ. *Environ Sci Technol* **2007,** *41*, (22), 7807-7817.
37. Henze, D. K.; Hakami, A.; Seinfeld, J. H., Development of the adjoint of GEOS-Chem. **2007**.
38. Yang, Y.-J.; Wilkinson, J. G.; Russell, A. G., Fast, direct sensitivity analysis of multidimensional photochemical models. *Environ Sci Technol* **1997,** *31*, (10), 2859-2868.
39. Hakami, A.; Odman, M. T.; Russell, A. G., High-order, direct sensitivity analysis of multidimensional air quality models. *Environ Sci Technol* **2003,** *37*, (11), 2442-2452.
40. Zhang, W.; Trail, M. A.; Hu, Y.; Nenes, A.; Russell, A. G., Use of high-order sensitivity analysis and reduced-form modeling to quantify uncertainty in particulate matter simulations in the presence of uncertain emissions rates: A case study in Houston. *Atmos Environ* **2015,** *122*, 103-113.
41. Itahashi, S.; Uno, I.; Kim, S., Seasonal source contributions of tropospheric ozone over East Asia based on CMAQ–HDDM. *Atmos Environ* **2013,** *70*, 204-217.
42. Zhang, W.; Capps, S.; Hu, Y.; Nenes, A.; Napelenok, S.; Russell, A., Development of the high-order decoupled direct method in three dimensions for particulate matter: enabling advanced sensitivity analysis in air quality models. *Geoscientific Model Development* **2012,** *5*, (2), 355-368.
43. Koo, B.; Dunker, A. M.; Yarwood, G., Implementing the decoupled direct method for sensitivity analysis in a particulate matter air quality model. *Environ Sci Technol* **2007,** *41*, (8), 2847-54.
44. Simon, H.; Baker, K. R.; Akhtar, F.; Napelenok, S. L.; Possiel, N.; Wells, B.; Timin, B., A direct sensitivity approach to predict hourly ozone resulting from compliance with the National Ambient Air Quality Standard. *Environ Sci Technol* **2013,** *47*, (5), 2304-2313.
45. Yarwood, G.; Emery, C.; Jung, J.; Nopmongcol, U.; Sakulyanontvittaya, T., A method to represent ozone response to large changes in precursor emissions using high-order sensitivity analysis in photochemical models. *Geoscientific Model Development* **2013,** *6*, (5), 1601-1608.
46. Zhang, Q.; Zheng, Y.; Tong, D.; Shao, M.; Wang, S.; Zhang, Y.; Xu, X.; Wang, J.; He, H.; Liu, W., Drivers of improved $PM_{2.5}$ air quality in China from 2013 to 2017. *Proceedings of the National Academy of Sciences* **2019,** *116*, (49), 24463-24469.
47. Liu, T.; Wang, C.; Wang, Y.; Huang, L.; Li, J.; Xie, F.; Zhang, J.; Hu, J., Impacts of model resolution on predictions of air quality and associated health exposure in Nanjing, China. *Chemosphere* **2020**, 126515.
48. Yarwood, G.; Sunja, R.; Mark, Y.; Gary Z., W. Updates to the Carbon Bond Chemical Mechanism: CB05.

696 <http://www.camx.com/publ/pdfs/cb05_final_report_120805.pdf>. (*accessed on* 02/28/2019).

697 49. Qin, M.; Yu, H.; Hu, Y.; Russell, A. G.; Odman, M. T.; Doty, K.; Pour-Biazar, A.; McNider, R. T.; Knipping,
698 E., Improving ozone simulations in the Great Lakes Region: The role of emissions, chemistry, and dry
699 deposition. *Atmos Environ* **2019,** *202*, 167-179.

700 50. Yu, S.; Mathur, R.; Sarwar, G.; Kang, D.; Tong, D.; Pouliot, G.; Pleim, J., Eta-CMAQ air quality forecasts for
701 O 3 and related species using three different photochemical mechanisms (CB4, CB05, SAPRC-99):
702 comparisons with measurements during the 2004 ICARTT study. *Atmospheric Chemistry and Physics* **2010,**
703 *10*, (6), 3001-3025.

704 51. Appel, K. W.; Napelenok, S. L.; Foley, K. M.; Pye, H. O.; Hogrefe, C.; Luecken, D. J.; Bash, J. O.; Roselle, S.
705 J.; Pleim, J. E.; Foroutan, H., Description and evaluation of the Community Multiscale Air Quality (CMAQ)
706 modeling system version 5.1. *Geoscientific Model Development* **2017,** *10*, (4), 1703-1732.

707 52. Cohan, D. S.; Hu, Y.; Russell, A. G., Dependence of ozone sensitivity analysis on grid resolution. *Atmos*
708 *Environ* **2006,** *40*, (1), 126-135.

709 53. Mathur, R.; Xing, J.; Gilliam, R.; Sarwar, G.; Hogrefe, C.; Pleim, J.; Pouliot, G.; Roselle, S.; Spero, T. L.;
710 Wong, D. C., Extending the Community Multiscale Air Quality (CMAQ) modeling system to hemispheric
711 scales: overview of process considerations and initial applications. *Atmospheric Chemistry and Physics* **2017,**
712 *17*, 12449.

713 54. United States Environmental Protection Agency Create Initial and Boundary Conditions from Seasonal
714 Average Hemispheric CMAQ Output.
715 <https://github.com/USEPA/CMAQ/blob/master/DOCS/Users_Guide/Tutorials/CMAQ_UG_tutorial_HCMA
716 Q_IC_BC.md>.

717 55. AiMa Forecasts AiMa air quality forecasting system. <http://www.aimayubao.com>. (*accessed on*
718 01/17/2020).

719 56. Lyu, B.; Zhang, Y.; Hu, Y., Improving $PM_{2.5}$ air quality model forecasts in China using a bias-correction
720 framework. *Atmosphere* **2017,** *8*, (8), 147.

721 57. Skamarock, W. C.; Klemp, J. B.; Dudhia, J.; Gill, D. O.; Barker, D. M.; Duda, M. G.; Huang, X.-Y.; Wang,
722 W.; Powers, J. G. *A description of the advanced research WRF version 3*; National Center For Atmospheric
723 Research Mesoscale and Microscale Meteorology Division: 2008.

724 58. National Centers for Environmental Prediction NCEP Products Inventory: Global Products, Global Forecast
725 System (GFS) Model. <https://www.nco.ncep.noaa.gov/pmb/products/gfs/#GFS>. (*accessed on* 05/17/2020).

726 59. Energy Statistics Division of National Bureau of Statistics, *China Energy Statistical Yearbook*. 2014.

727 60. Lyu, B.; Hu, Y.; Zhang, W.; Du, Y.; Luo, B.; Sun, X.; Sun, Z.; Deng, Z.; Wang, X.; Liu, J.; Wang, X.; Russell,
728 A. G., Fusion Method Combining Ground-Level Observations with Chemical Transport Model Predictions
729 Using an Ensemble Deep Learning Framework: Application in China to Estimate Spatiotemporally-Resolved
730 $PM_{2.5}$ Exposure Fields in 2014-2017. *Environ Sci Technol* **2019,** *53*, (13), 7306-7315.

731 61. Lyu, B.; Zhang, Y.; Hu, Y., Improving $PM_{2.5}$ Air Quality Model Forecasts in China Using a Bias-Correction
732 Framework. *Atmosphere* **2017,** *8*, (8), 147.

733 62. Zhang, Q.; Streets, D. G.; Carmichael, G. R.; He, K. B.; Huo, H.; Kannari, A.; Klimont, Z.; Park, I. S.; Reddy,
734 S.; Fu, J. S.; Chen, D.; Duan, L.; Lei, Y.; Wang, L. T.; Yao, Z. L., Asian emissions in 2006 for the NASA
735 INTEX-B mission. *Atmos Chem Phys* **2009,** *9*, (14), 5131-5153.

736 63. Zheng, B.; Tong, D.; Li, M.; Liu, F.; Hong, C.; Geng, G.; Li, H.; Li, X.; Peng, L.; Qi, J.; Yan, L.; Zhang, Y.;
737 Zhao, H.; Zheng, Y.; He, K.; Zhang, Q., Trends in China's anthropogenic emissions since 2010 as the
738 consequence of clean air actions. *Atmos Chem Phys* **2018,** *18*, (19), 14095-14111.

739 64. China National Environmental Monitoring Center China National Urban Air Quality Real-Time Publishing
740 Platform. <http://www.cnemc.cn/>. (*accessed on* 05/14/2020).

741 65. Hu, J.; Chen, J.; Ying, Q.; Zhang, H., One-year simulation of ozone and particulate matter in China using
742 WRF/CMAQ modeling system. *Atmos Chem Phys* **2016,** *16*, (16), 10333-10350.

743 66. Hu, J.; Li, X.; Huang, L.; Ying, Q.; Zhang, Q.; Zhao, B.; Wang, S.; Zhang, H., Ensemble prediction of air
744 quality using the WRF/CMAQ model system for health effect studies in China. *Atmos Chem Phys* **2017,** *17*,
745 (21), 13103-13118.

746 67. Kong, L.; Tang, X.; Zhu, J.; Wang, Z.; Fu, J. S.; Wang, X.; Itahashi, S.; Yamaji, K.; Nagashima, T.; Lee, H.-J.;
747 Kim, C.-H.; Lin, C.-Y.; Chen, L.; Zhang, M.; Tao, Z.; Li, J.; Kajino, M.; Liao, H.; Wang, Z.; Sudo, K.; Wang,
748 Y.; Pan, Y.; Tang, G.; Li, M.; Wu, Q.; Ge, B.; Carmichael, G. R., Evaluation and uncertainty investigation of
749 the NO_2, CO and NH_3 modeling over China under the framework of MICS-Asia III. *Atmos Chem Phys* **2020,**
750 *20*, (1), 181-202.

751 68. Grant, A.; Archibald, A. T.; Cooke, M. C.; Shallcross, D. E., Modelling the oxidation of seventeen volatile
752 organic compounds to track yields of CO and CO_2. *Atmos Environ* **2010,** *44*, (31), 3797-3804.

753 69. Zhang, H.; Yee, L. D.; Lee, B. H.; Curtis, M. P.; Worton, D. R.; Isaacman-VanWertz, G.; Offenberg, J. H.;
754 Lewandowski, M.; Kleindienst, T. E.; Beaver, M. R.; Holder, A. L.; Lonneman, W. A.; Docherty, K. S.; Jaoui,

M.; Pye, H. O. T.; Hu, W.; Day, D. A.; Campuzano-Jost, P.; Jimenez, J. L.; Guo, H.; Weber, R. J.; de Gouw, J.; Koss, A. R.; Edgerton, E. S.; Brune, W.; Mohr, C.; Lopez-Hilfiker, F. D.; Lutz, A.; Kreisberg, N. M.; Spielman, S. R.; Hering, S. V.; Wilson, K. R.; Thornton, J. A.; Goldstein, A. H., Monoterpenes are the largest source of summertime organic aerosol in the southeastern United States. *Proc Natl Acad Sci USA* **2018,** *115*, (9), 2038-2043.

70. Zhao, B.; Wang, S.; Donahue, N. M.; Jathar, S. H.; Huang, X.; Wu, W.; Hao, J.; Robinson, A. L., Quantifying the effect of organic aerosol aging and intermediate-volatility emissions on regional-scale aerosol pollution in China. *Sci Rep* **2016,** *6*, (1), 28815.
71. Tie, X.; Brasseur, G.; Emmons, L.; Horowitz, L.; Kinnison, D., Effects of aerosols on tropospheric oxidants: A global model study. *Journal of Geophysical Research: Atmospheres* **2001,** *106*, (D19), 22931-22964.
72. Tie, X., Assessment of the global impact of aerosols on tropospheric oxidants. *Journal of Geophysical Research* **2005,** *110*, (D3), 204.
73. George, I. J.; Abbatt, J. P., Heterogeneous oxidation of atmospheric aerosol particles by gas-phase radicals. *Nat Chem* **2010,** *2*, (9), 713-22.
74. Chapleski, R. C.; Zhang, Y.; Troya, D.; Morris, J. R., Heterogeneous chemistry and reaction dynamics of the atmospheric oxidants, O_3, NO_3, and OH, on organic surfaces. *Chem Soc Rev* **2016,** *45*, (13), 3731-46.
75. Rose, A. N.; McKee, J. J.; Urban, M. L.; Bright, E. A., LandScan 2017. In 2017 ed.; Oak Ridge National Laboratory: Oak Ridge, TN, 2018.
76. Sibson, R., A brief description of natural neighbour interpolation. *Interpreting Multivariate Data* **1981**.
77. Huang, Z.; Hu, Y.; Zheng, J.; Yuan, Z.; Russell, A. G.; Ou, J.; Zhong, Z., A New Combined Stepwise-Based High-Order Decoupled Direct and Reduced-Form Method To Improve Uncertainty Analysis in $PM_{2.5}$ Simulations. *Environ Sci Technol* **2017,** *51*, (7), 3852-3859.
78. Ministry of Ecology and Environment of the People's Republic of China, Ambient Air Quality Standards. In 2016; Vol. GB 3095—2012.
79. Ministry of Ecology and Environment of the People's Republic of China Announcement on issuing the amendment of "Ambient Air Quality Standards" (GB 3095-2012). <http://www.mee.gov.cn/gkml/sthjbgw/sthjbgg/201808/t20180815_451398.htm>. (*accessed on* 06/14/2020).
80. United States Environmental Protection Agency Air Quality Design Values. <https://www.epa.gov/air-trends/air-quality-design-values>. (*accessed on* 02/15/2019).
81. Li, M.; Liu, H.; Geng, G.; Hong, C.; Liu, F.; Song, Y.; Tong, D.; Zheng, B.; Cui, H.; Man, H., Anthropogenic emission inventories in China: a review. *National Science Review* **2017,** *4*, (6), 834-866.
82. National Bureau of Statistics of China, *China Statistical Yearbook 2019*. China Statistics Press: 2019.
83. Statistical Bureau of Guangdong, *Guangdong Statistical Yearbook 2017*. China Statistics Press: 2017.
84. Shen, H. Z.; Tao, S.; Chen, Y. L.; Ciais, P.; Guneralp, B.; Ru, M. Y.; Zhong, Q. R.; Yun, X.; Zhu, X.; Huang, T. B.; Tao, W.; Chen, Y. C.; Li, B. G.; Wang, X. L.; Liu, W. X.; Liu, J. F.; Zhao, S. Q., Urbanization-induced population migration has reduced ambient $PM_{2.5}$ concentrations in China. *Science Advances* **2017,** *3*, (7), e1700300.
85. Statistical Bureau of Sichuan, *Sichuan Statistical Yearbook 2017*. China Statistics Press: 2017.
86. State Council of the People's Republic of China Notice of the general office of the state council on issuing the air pollution prevention and control action plan. <http://www.gov.cn/zwgk/2013-09/12/content_2486773.htm>. (*accessed on* 03/24/2020).
87. Wang, N.; Lyu, X.; Deng, X.; Huang, X.; Jiang, F.; Ding, A., Aggravating O_3 pollution due to NO*x* emission control in eastern China. *Sci Total Environ* **2019,** *677*, 732-744.
88. Li, Y.; Lau, A. K. H.; Fung, J. C. H.; Zheng, J.; Liu, S., Importance of NO*x* control for peak ozone reduction in the Pearl River Delta region. *Journal of Geophysical Research: Atmospheres* **2013,** *118*, (16), 9428-9443.
89. Jacob, D. J.; Winner, D. A., Effect of climate change on air quality. *Atmos Environ* **2009,** *43*, (1), 51-63.
90. Zhao, S.; Yin, D.; Yu, Y.; Kang, S.; Qin, D.; Dong, L., $PM_{2.5}$ and O_3 pollution during 2015-2019 over 367 Chinese cities: Spatiotemporal variations, meteorological and topographical impacts. *Environ Pollut* **2020,** *264*, 114694.
91. Zhang, Y. L.; Cao, F., Fine particulate matter ($PM_{2.5}$) in China at a city level. *Sci Rep* **2015,** *5*, (1), 14884.
92. Feng, J.; Quan, J.; Liao, H.; Li, Y.; Zhao, X., An Air Stagnation Index to Qualify Extreme Haze Events in Northern China. *Journal of the Atmospheric Sciences* **2018,** *75*, (10), 3489-3505.
93. Wang, Y.; Wang, H.; Wang, W., A Stratospheric Intrusion-Influenced Ozone Pollution Episode Associated with an Intense Horizontal-Trough Event. *Atmosphere* **2020,** *11*, (2), 164.
94. Xu, W.; Lin, W.; Xu, X.; Tang, J.; Huang, J.; Wu, H.; Zhang, X., Long-term trends of surface ozone and its influencing factors at the Mt Waliguan GAW station, China – Part 1: Overall trends and characteristics. *Atmos Chem Phys* **2016,** *16*, (10), 6191-6205.

95. Li, D.; Bian, J.; Fan, Q., A deep stratospheric intrusion associated with an intense cut-off low event over East Asia. *Science China Earth Sciences* **2014,** *58*, (1), 116-128.

96. Zhao, Y.; Zhang, K.; Xu, X.; Shen, H.; Zhu, X.; Zhang, Y.; Hu, Y.; Shen, G., Substantial Changes in Nitrogen Dioxide and Ozone after Excluding Meteorological Impacts during the COVID-19 Outbreak in Mainland China. *Environmental Science & Technology Letters* **2020,** *7*, (6), 402-408.